In-Situ Anchoring Co-N-C Nanoparticles on Co_4N Nanosheets towards Ultrastable Flexible Self-Supported Bifunctional Oxygen Electrocatalyst Enables Recyclable Zn-Air Batteries over 10000 Cycles and Fast-Charging

Tong Liu[a], Siyuan Zhao[a], Ying Wang[b], Jie Yu[a], Yawen Dai[a], Jian Wang[a], Xiaoxu Sun,[c] Kaihua Liu[d], Meng Ni[a]*

Dr. T. Liu, S. Zhao, Dr. J. Yu, Y. Dai, Dr. J. Wang, Prof. Ni,
[a] Building Energy Research Group, Department of Building and Real Estate, Research Institute for Sustainable Urban Development (RISUD) and Research Institute for Smart Energy (RISE), The Hong Kong Polytechnic University, Hung Hom, Kowloon 999077, Hong Kong, China
Email: meng.ni@polyu.edu.hk

Dr. Y. Wang,
[b] State Key Laboratory of Rare Earth Resource Utilization, Changchun Institute of Applied Chemistry Chinese Academy of Sciences, Changchun 130022, China

Dr. X. Sun
[c]Jiangsu Collaborative Innovation Centre of Biomedical Functional Materials, Jiangsu Key Laboratory of New Power Batteries, School of Chemistry and Materials Science, Nanjing Normal University, Nanjing 210023, China

Dr. K. Liu,
[d] School of Chemistry and Chemical Engineering, Yantai University, Yantai 264005, China

Keywords: Zn-air batteries, ORR/OER, recyclable, fast-charing, flexible batteries

Zn-air batteries (ZABs) are very promising for flexible energy storage, but their application is limited to the primary battery. Developing the efficient and non-noble metal cathode toward oxygen reduction/evolution reactions (ORR/OER) is of great significance for the commercial application of rechargeable ZABs. Herein, a flexible self-supported integrated bifunctional cathode in which the Co-N-C nanoparticles were in-situ anchored on Co_4N nanosheets via a facile and scalable strategy. Benefiting from integrated three-dimensional architecture with adequate active sites, porous structure, high conductivity originating from the metal substrate, and the synergistic effects of Co-N-C and Co_4N, the cathode exhibits excellent bifunctional activity (low overpotential of 275 mV at 10 mA cm^{-2} for OER, high half-wave potential of 0.833 V for ORR), and ultralong durability for ORR/OER in the alkaline medium. Impressively, this cathode enables the recyclable aqueous ZABs a record overall lifespan over 10000 cycles at 20 mA cm^{-2}, and a superior fast-charging feature at an ultrahigh charging current density of 100 mA cm^{-2}. Furthermore, such a flexible integrated cathode can be directly used as a self-supported cathode for the flexible solid-state ZABs, with excellent reversibility for 300 cycles, demonstrating its feasibility for practical application.

1. Introduction

The fast development of wearable electronics requires flexible energy storage devices that is lightweight, deformable, stretchable, and with high energy density.[1-4] Although some flexible battery prototypes have been proposed, they still cannot satisfy the high demand of scalable and high-performance limited by the complex processes, low throughput, and high cost.[5-7] Among various novel flexible batteries, the aqueous rechargeable flexible Zinc-air battery (ZAB) with a semi-open structure is a promising candidate due to the high energy density of 1086 Wh kg^{-1}, high power density, low cost, environmentally friendliness, and high safety.[8-12] However, most of the reported ZABs are severely limited by the cycling performance and energy efficiency, resulting from the Zn dendrite formation and sluggish cathodic oxygen reduction/evolution reaction (ORR/OER).[13,14] Moreover, the long charging time of flexible batteries severely hindered their real applications for wearable electronics, and thus fast charging capability has become one of the key requirements.[15] The current application of ZAB is still limited to primary battery commonly applied in small devices such as hearing aids, let alone the fast-charging features. Although significant progress has been achieved on cathodes, developing ideal bifunctional air electrodes that are active for ORR and OER is yet challenging for realizing high-performance flexible ZABs.[16,17]

At present, the benchmark catalysts for ORR and OER are Pt-based and Ir/Ru-based composites, respectively. Nevertheless, their single electrocatalytic activity for either ORR or OER, scarcity, high cost, and declining stability limit their use on a large scale.[18-21] In this context, transition metallic compounds (TMCs) were ideal alternatives for noble metal electrocatalysts due to their earth-abundant nature and high catalytic activity.[22-24] Co-nitrogen-carbon (Co-N-C) have been regarded as a promising substitute for Pt-based catalysts, owing to their earth-abundant nature and high ORR catalytic activity.[25,26] Co_4N possessed both metallic Co-Co and covalent Co-N interactions, displaying metallic features and preferred OER activity arising from the contraction of the d band.[27,28] In theory, a cathode composed of Co-N-C with Co_4N could be

an efficient bifunctional OER/ORR electrode for ZABs, which is considered attractive, but how to combine them via a facile strategy is very challenging.[17,29,30]

Metal-organic frameworks (MOFs) with intriguing structures, exceptional porosity, and multifunctional properties were widely used as precursors/templates to fabricate porous M-N-C (M=Fe, Co, Cu, Zn, etc).[31] However, most of the obtained M-N-C derived from MOFs were prepared by direct pyrolysis at high temperatures, rendering the inevitable aggregation of particles and thus resulting in damaging of porous structure, decreasing reactant transfer, and poor electronic conductivity.[32-34] In addition, the traditional cathode preparation method is obtained by spraying a slurry mixed with additive carbon material and a binder on a flexible substrate, which could cause detachment of active catalysts from substrates caused by the gas bubbling/evolution during the reaction and repeated external deformations.[16,35-37] Moreover, the addition of readily corroded conductive carbon and the insulating binder would cause a decrease in the cathode performance.[38-40] To this end, constructing a carbon/binder-free cathode by in situ anchoring the Co-N-C on the functional supports such as Co_4N could simultaneously fulfil these challenging requirements.[41-45]

With these purposes in mind, a flexible self-supported integrated bifunctional SSM/Co_4N/CoNC oxygen electrocatalyst was fabricated on the via a facile and scalable strategy. After pyrolysis with melamine at low temperature, the in-situ grown nanosheets that served as functional substrates were derived to Co_4N, the followed grafted ZIF-67 nanoparticles conversed to the Co-N-C. Benefiting from the tremendous active sites, high electron conductivity from the intimate contact, hierarchical porous structures for the rapid transformation of intermediate, synergistic effects between noble metal-free Co_4N and Co-N-C, the resultant integrated cathode demonstrated impressive bifunctional catalytic activities for ORR/OER. The SSM/Co_4N/CoNC also enabled the conventional aqueous ZABs and flexible solid-state ZABs high rate performance, fast-charging capability and exceptional durability, showing the potential for application in wearable electronics.

2. Results and Discussion

The facile synthesis progress of the flexible SSM/Co_4N/CoNC cathode was presented in **Figure 1a**. The stainless steel mesh (noted as SSM, Figure S1), with the features of excellent conductivity (Figure S2, Table S1), robust mechanical strength and low cost, was considered as a good flexible support to grow active catalysts for electrochemical energy storage devices. Firstly, immersed the SSM in cobalt nitrate hexahydrate and urea solution to grow nanosheets on it by a mild hydrothermal reaction. As presented in Figure 1b and Figure S3, the nanosheets with higher specific surfaces were uniformly dispersed on the SSM, giving the SSM/Co_4N/CoNC electrode more mass transfer capability and more exposed active sites than the SSM/CoNC that directly grown ZIF-67 derived CoNC on the bare SSM (Figure S4). Secondly, in-situ grown the ZIF-67 nanoparticles in a methanol solution containing $Co(NO_3)_2 \cdot 6H_2O$ and 2-methylimidazole. The Co^{2+} ion in nanosheets provided sufficient nucleation sites for the growth of ZIF-67, ensuring its large and homogeneous distribution (Figure 1c,d, Figure S5). Thirdly, the precursor was heated in the N_2-filled tube furnace at a temperature of 400 °C, wherein the melamine was sacrificed as carbon and nitrogen sources to obtain the SSM/Co_4N/CoNC cathode. It should be noted that the polyhedral morphology of ZIF-67 nanoparticles and $Co(OH)_2$ nanosheets were well reserved after pyrolysis, which could be derived from low reaction temperature avoiding structural damage and aggregation (Figure 1e-g, Figure S6). Figure S7 schematically exhibited the evolution of ZIF-67 nanoparticles that in-situ grown on the nanosheets, which was confirmed by the immature dodecahedrons in Figure S8. After calcination, the in-situ grown nanoparticles were tightly anchored on the nanosheets forming a self-supported integrated structure, which is beneficial for the stability of the cathodes. It is noted that there are many pores generated after heating, which is supported by the pore volume of 0.25 $cm^3\ g^{-1}$ for SSM/Co_4N/CoNC (Figure S9). The porous surface with a large BET surface area of 102.6 $m^2\ g^{-1}$ can provide plenty of catalytic sites and improve electrode-electrolyte contact, which is beneficial to boost the electrocatalytic reaction.

According to element mappings (**Figure 2a**), the elements of Co, C, N were uniformly distributed on the cathode surface, displaying the Co-N-C present on SSM/Co_4N/CoNC oxygen electrocatalyst. Transmission electron microscopy (TEM) images also confirmed the SSM/Co_4N/CoNC obtained porous features after the pyrolysis (Figure 2b,c). The inset of high-resolution TEM exhibited a distinct lattice fringe of 0.207 nm, corresponding to the (111) plane of the Co_4N, which was verified by the X-ray diffraction (XRD) patterns. As SSM substrates possessed high crystallization (Figure S10), we tested XRD pattern of the powders scraped from SSM/Co_4N/CoNC to exclude the effect from SSM. The XRD result of powders displayed two peaks centered at approximately 43.7 ° and 50.8 °, corresponding to (111) and (200) diffractions for Co_4N, manifesting the successful formation of Co_4N (Figure 2d). However, there was no obvious XRD reflection peak of Co-N-C detected for SSM/Co_4N/CoNC, which might be due to the strong crystallization of Co_4N and poor crystallization of C prepared at the relatively low pyrolysis temperature. After etching by 0.5M sulfuric acid to eliminate the influence of Co_4N, SSM/Co_4N/CoNC-acid powders exhibited the apparent peak of C, demonstrating the generation of Co-N-C in SSM/Co_4N/CoNC cathode. For comparison, the XRD patterns in Figure S11 confirmed the formation of Co_4N for SSM/Co_4N-powders and the Co-N-C for SSM/CoNC-powders, respectively. The elemental composition and chemical state of the SSM/Co_4N/CoNC were studied by X-ray photoelectron spectroscopy (XPS). As the Co 2p XPS spectra shown in Figure 2e, the peaks centred at 778.3 and 795.9 eV corresponded to 2p3/2 and 2p1/2 of zero-valence state Co, indicating the presence of Co-Co bonds. Peaks at 781.3 and 797.4 eV were assigned to the ionic state Co, that is, Co-N bonds.[46,47] Two concomitant peaks detected at 786.0 and 803.0 eV were attributed to the satellite peaks. This result was consistent with the two kinds of binding states for Co in Co_4N. The peak located at 398.9 eV in the N1s XPS spectrum (Figure 2f) revealed that N species exist as Co-N bonds. It may be attributed to the Co_4N and the Co-N-C that derived from the Co-linker nodes in ZIF-67. The graphitic-N

observed at 400.6 eV can affect the geometric and electronic structure of the carbon and reveal a positive function towards ORR.[48] In addition, the peaks of 287.0 and 287.8 eV in the C 1s spectrum confirmed the carbon atom bonding with N (Figure 2g), further proving the existence of Co-N-C in SSM/Co_4N/CoNC.[49] The coexistence of Co_4N and Co-N-C was also confirmed by the Raman spectrum and FTIR spectrum. As the Raman spectrum shown in Figure 2h, SSM/Co_4N/CoNC and SSM/Co_4N cathodes exhibited pointed peaks at E_g (482 cm^{-1}), F_{2g} (513 and 619 cm^{-1}), and A_{1g} (689 cm^{-1}) vibration modes of Co elements, suggesting the formation of Co_4N.[50,51] On the contrary, only a barely visible peak among 560 to 695 cm^{-1} were detected in the spectrum of SSM/CoNC. Furthermore, two characteristic peaks corresponding to D and G bands of graphite were observed at 1336 and 1599 cm^{-1}, confirming the formation of Co-N-C for SSM/Co_4N/CoNC and SSM/CoNC cathodes. The FTIR spectrum in Figure 2i proved the SSM/Co_4N/CoNC cathode well consists of the Co_4N in SSM/Co_4N and Co-N-C in SSM/CoNC. All these results manifested the proposed strategy is effective to fabricate the self-supported SSM/Co_4N/CoNC cathode with combined the Co_4N nanosheets and Co-N-C nanoparticles. It should be noted that the flexible SSM/Co_4N/CoNC electrode produced using this strategy is as large as 200 cm^2, which can be directly applied to large-size batteries (Figure S12). Moreover, the SSM/Co_4N/CoNC electrode could bear a weight of 500 g, demonstrating high mechanical strength, which could satisfy the demand in practical applications (Figure S13). In short, the strategy proposed here is successful, and the cathode with the unique architecture is believed to play a notable role in the subsequent ORR and OER tests.

The integrated SSM/Co_4N/CoNC cathode directly served as a working electrode and was evaluated by a three-electrode system in the 1M KOH electrolyte to verify its OER electrocatalytic activities. For comparison, electrochemical performances of SSM/Co_4N without ZIF-67 nanoparticles, SSM/CoNC without nanosheets, Co_4N/CoNC without SSM substrate, Pt/C, and RuO_2 were tested. We evaluated the OER activity of the cathodes based on the overpotential at the current density of 10 mA cm^{-2} (E_J=10). The SSM/Co_4N/CoNC cathode

delivered a potential of 1.50 V at 10 mA cm^{-2} (**Figure 3a**), significantly lower than SSM/Co_4N (1.53 V), SSM/CoNC (1.57 V), Co_4N/CoNC (1.55 V), RuO_2 (1.53 V), and Pt/C (1.62 V), manifesting excellent OER activity of SSM/Co_4N/CoNC. The lower OER overpotential of 275 mV for SSM/Co_4N/CoNC than SSM/Co_4N and SSM/CoNC could be attributed to the effective synergistic effect between Co_4N and CoNC. Notely, the SSM/Co_4N/CoNC also demonstrated a lower OER overpotential than Co_4N/CoNC, which can be ascribed to the self-supported porous architecture without the binder and additive carbon. The excellent OER performance of SSM/Co_4N/CoNC was derived from its lowest Tafel slope (32.11 mV dec^{-1}) compared to other counterparts (34.42 mV dec^{-1} for Co_4N/CoNC, 45.54 mV dec^{-1} for SSM/Co_4N, 77.45 mV dec^{-1} for SSM/CoNC, 68.00 mV $dec^{-1}$for RuO_2, and 99.53 mV dec^{-1} for Pt/C), implying the fastest OER kinetics. The favourable OER kinetics of SSM/Co_4N/CoNC than Co_4N/CoNC could further prove the merit of the designed binder-free self-supported structure that can afford efficient mass transport, thus promoting reaction kinetics. The improved OER performance is believed to come from the increased accessible surface area: the active nanosheets can notably improve the loading amount of ZIF-67 compared to the bare SSM substrates; the ZIF-67 nanoparticles with polyhedral structure exposed more active sites for OER; which was proved by the electrochemical double-layer capacitance (C_{dl}). The C_{dl} of SSM/Co_4N/CoNC was 19.39 mF cm^{-2} (Figure 3c, Figure S14), which is remarkably higher than that of SSM/Co_4N (0.98 mF cm^{-2}) and SSM/CoNC (0.11 mF cm^{-2}), indicating that SSM/Co_4N/CoNC has a larger active surface area. Besides the low overpotential, the long-term durability is also of great significance for the practical applications of electrodes in energy storage devices. As revealed in Figure 3d, after 1000 continuous cyclic voltammetry cycles, the polarization curve shows negligible decline. The hierarchically integrated structure was also well reserved (Figure 3e,f), in which the nanoparticles were still uniformly dispersed on the nanosheets, suggesting the stability of SSM/Co_4N/CoNC. Afterwards, we tested the OER durability of cathodes at 10 mA cm^{-2}. As shown in Figure 3g, the potential of Pt/C electrode increased rapidly only 5 hours later, and that

of RuO_2 demonstrated rising in 25 hours. By comparison, the voltage of SSM/Co_4N/CoNC was highly stable, which merely increase from 1.504 V to 1.517 V after 300 hours, further indicating the ultra long-term durability. The superior durability mainly originated from the intimate contact between electrocatalysts and conductive substrates, which could provide high electron conductivity and efficiently hinder the mechanical shedding of catalysts from substrates throughout sustained O_2 evolution. Of note, The electrolyte for SSM/Co_4N/CoNC was still colourless transparent, yet RuO_2 and Pt/C were turned into brown caused by conductive carbon and binder oxidation (Figure 3h, Figure S15). The electrolyte color is unchanged which suggest no detached active substance is peeled from the SSM, demonstrating the excellent stability of SSM/Co_4N/CoNC. This excellent staiblity could be attributed to the electrode that was in-situ grown on the SSM conductive substrates without the addition of polymer binders and conductive additives carbon. The above results revealed the superiority of self-supported structure and additive carbon/binder-free.

To evaluate the bifunctional performance of SSM/Co_4N/CoNC oxygen electrocatalyst, its ORR catalytic activity, which is significantly important for employing in ZABs, was further investigated. To avoid the effect of oxygen diffusion, the rotating disk electrode was used to investigate the ORR performances in an O_2-saturated 0.1 M KOH electrolyte. The self-supported SSM/Co_4N/CoNC electrode was scraped to obtain the powdery catalyst for dipping. As displayed in **Figure 4a**, the SSM/Co_4N/CoNC exhibited a half-wave potential ($E_{1/2}$) of 0.833 V compared to Pt/C (0.853 V) and RuO_2 (0.67 V). Tafel slope of SSM/Co_4N/CoNC was 92.4 mV dec^{-1} (Figure 4b), which is close to commercial Pt/C catalyst (90.62 mV dec^{-1}) and lower than RuO_2 (113.14 mV dec^{-1}), indicating a rapid ORR kinetics of SSM/Co_4N/CoNC. Its electrocatalytic kinetics towards ORR was also examined by rotating disk measurements at different rotating speeds (Figure 4c). Koutecky-Levich (K-L) plots in Figure 4d and Figure S18 for the potential range from 0.2 to 0.5 V indicated linear relationships, implying first-order reaction kinetics for SSM/Co_4N/CoNC oxygen electrocatalyst. The calculated electron transfer

number (*n*) for RuO_2 was less than 4.0 at various potentials related to the $2e^-$ ORR catalytic pathway (Figure 4e). By contrast, *n* for SSM/Co_4N/CoNC was calculated to 4.0 at different potentials, consistent with that of Pt/C, confirming O_2 was reduced by an efficient $4e^-$ pathway. As shown in Figure 4f and Figure S19, after a 10h chronoamperometric test carried out at the constant voltage of 0.5 V (vs RHE) under a rotating speed of 1600 rpm, SSM/Co_4N/CoNC displayed an ORR current of 98.24% compared to its pristine, considerably higher than those of RuO_2 (80.47 %) and Pt/C (67.54 %), exhibiting its excellent ORR durability. The superior ORR performance and durability of SSM/Co_4N/CoNC may derive from the integrated structure with immense advantages, therefore could guarantee high electron transfer and efficient oxygen diffusion on the larger active surface area.

The bifunctional activitieps of electrocatalytic catalysts were assessed by the potential gap between OER and ORR metrics ($\Delta E = E_{J=10} - E_{1/2}$), as shown in Figure 4g. The SSM/Co_4N/CoNC demonstrated a ΔE value of 0.67 V, drastically lower than RuO_2 (0.86 V) and Pt/C (0.77 V) electrodes, which is also smaller than the recently published cathodes (Figure 4h, Table S2). In short, its remarkable bifunctional activity and ultrastable durability for OER and ORR could be ascribed to the following features: integrated three-dimensional architecture with adequate catalytic sites and improved active area, hierarchically porous structure, high conductivity originated from the metal substrate and self-supported structure, reduced side reactions due to without the addition of inactive additives, and synergistic effects between Co_4N and Co-N-C. The synergistic effects may originate from the increased electronic interaction between Co_4N and Co-N-C due to the Lewis acid feature of Co and the Lewis base feature of the N-C. The Lewis acid originated from Co ions possess the empty orbit outside the nucleus. It could accept the electronic pairs from OH_x moieties (aqua, hydroxo, etc.) and boost the catalytic activity towards OER.[52,53] The Lewis base that N-doped carbon derived from ZIF-67, can adsorb O_2 molecules owing to the possibility of electron pair donation and hence promoting the ORR.[54,55]

Considering its remarkable bifunctional OER/ORR activity, the SSM/Co_4N/CoNC was performed as the air cathode to explore its performance in rechargeable aqueous ZAB. As shown in **Figure 5a**, at 10 mA cm^{-2}, the SSM/Co_4N/CoNC cathode exhibited a high specific capacity of 773.9 mAh g^{-1} (based on the consumed Zn), which exceeded the RuO_2 (620.6 mAh g^{-1}) and Pt/C (659.0 mAh g^{-1}). It is noted that the voltage plateau of SSM/Co_4N/CoNC is always higher than RuO_2 and Pt/C during the discharge progress. The lower polarization of self-supported SSM/Co_4N/CoNC indicated the superiority to the sprayed noble metal electrodes. As presented in Figure 5b, compared with RuO_2 and Pt/C, the SSM/Co_4N/CoNC-based ZAB displayed a lower charge-discharge voltage gap (1.05 V at 50 mA cm^{-2}), a higher operating current density and the highest peak power density (105 mW cm^{-2}). Figure 5c exhibited the galvanostatic cycling curves at a series of current densities to evaluate the overpotentials variation of batteries at different current densities. The voltage gap of SSM/Co_4N/CoNC-based ZAB increased from 0.67 to 0.91 V as current densities risen from 1 to 20 mA cm^{-2}, much lower than the RuO_2 and Pt/C (Figure S20), implying its extraordinary rate performance. In addition, the discharge and charge voltages of ZAB with SSM/Co_4N/CoNC cathode retained more steady than those of Pt/C and RuO_2 cathodes after current density returned, which also manifesting superb durability of SSM/Co_4N/CoNC. We took galvanostatic charge-discharge tests to assess the cycling performance of ZABs. Impressively, SSM/Co_4N/CoNC-based ZAB can cycle over 2700 times (900 h) with relatively stable discharge-charge voltages at 10 mA cm^{-2} and 20 min each cycle (Figure 5d). Besides, its voltage gap only increased from 0.77 V to the ultimate 0.83 V, far outperforming the ZABs with RuO_2 and Pt/C cathodes, which displayed an incredible discharge and charge voltage variation. Stimulated by the increasing interest in fast-charging batteries in recent years and the outstanding charing performance of SSM/Co_4N/CoNC cathode under high current density, the SSM/Co_4N/CoNC-based ZAB was discharged at 20 mA cm^{-2} and charged at 100 mA cm^{-2}. As shown in Figure 5e, the battery displayed excellent fast-charging features for more than 1750 cycles (350 h), and the overpotential was consistent at

0.89 V. The excellent stability of ZAB even under a high charge current density demonstrated the great potential application of SSM/Co_4N/CoNC for fast-charging batteries.

Inspired by the SSM/Co_4N/CoNC-based ZAB has super stable cycling performance even in the terminal, the premature death of ZAB may not caused by the fail of SSM/Co_4N/CoNC cathode. To reveal the failure mechanism, we take out and analyzed the Zn plate from the failed ZAB for analysis. It should be noted that the Zn anode was almost exhausted (inset in **Figure 6a)**.The poor reversibility of Zn anode was caused by the growth of dendritic zinc and the formation of dead zinc.[56-60] The SEM images illustrated, after numerous cycles, the surface morphology of the Zn anode also turned much rougher than that of the original anode (Figure 6a, Figure S21). XRD curves revealed many ZnO generated on the Zn anode after long-term cycles, confirming its severe corrosion (Figure 6b, Figure S23). Moreover, ZAB reconstituted with recovered SSM/Co_4N/CoNC , and fresh anode/electrolyte could still be recycled another 2400 times at 10 mA cm^{-2} (Figure 6c), further suggesting that the Zn anode limited the battery reversibility rather than the designed SSM/Co_4N/CoNC cathode. The low voltage gap of 0.77 V and long cycling lifespan further indicated the ultrastable stability of the SSM/Co_4N/CoNC cathode. Inspired from the excellent performance, we then tested a ZAB using SSM/Co_4N/CoNC cathode and two times the mass of zinc anode at a high current density of 20 mA cm^{-2}. As expected, the battery could steady cycle for more than 970h with a voltage gap slightly increased from 0.84 V to 0.91 V(Figure 6d). Furthermore, we assembled the recyclable ZAB based on the used SSM/Co_4N/CoNC cathode after cycles accompanied by repeatedly renewed Zn anode and electrolyte. Surprisingly, the rebuilt ZAB demonstrated a remarkable overall lifespan of more than 10000 cycles (3350h) based on one SSM/Co_4N/CoNC cathode. To the best of our knowledge, the lifespan of 970h in a rechargeable ZAB is a noteworthy performance (Figure 6e, Table S3), while the 3350h for the recyclable ZAB is a new record. Furthermore, the reconstituted fast-charing ZAB based on used SSM/Co_4N/CoNC cathode can also cycle steadily for more than 2300 times at the high charging current of 100 mA cm^{-2}, proving that the

fabricated SSM/Co_4N/CoNC cathode possessed excellent durability (Figure 6f). It is worth noting that the SSM/Co_4N/CoNC cathode has successfully made the applicable working conditions of rechargeable ZABs reach ultra-stable cycle life and ultrahigh charging current, which represents the state-of-the-art ZAB techniques.

As SSM/Co_4N/CoNC cathode has excellent bifunctional catalytic activity for OER/ORR, self-supported structure, robust and conductive substrates, and scalable features, a flexible solid-state ZAB was manufactured to verify its performance in practical applications in flexible devices. The schematic in **Figure 7a** presented the rechargeable solid-state ZAB composed of Zn foil anode, alkaline polyvinyl alcohol (PVA) solid-state electrolyte, and SSM/Co_4N/CoNC cathode. As shown in Figure 7b, the obtained pouch-type ZAB with large size of over 30×4 cm^2 (Figure S22) was intentionally bent and twisted to evaluate their flexibility. It is noteworthy the flexible ZAB exhibited a stable open-circuit voltage under various deformations. In addition, discharge-charge curves in Figure 7c showed they were stable under different bending angles, further indicating that the flexible ZABs with the SSM/Co_4N/CoNC has good mechanical flexibility and stability. This outstanding flexibility can be attributed to the flexible SSM substrate, giving the battery robustness and high conductivity even under deformations. The solid-state ZAB with SSM/Co_4N/CoNC cathode (inset in Figure 7d) presented a stable lifespan of 300 cycles (100 h) with an initial voltage gap of 0.96 V, and the terminal voltage gap increased a little to 0. 99 V at 1 mA cm^{-2} (Figure 7d, Figure S24). It still can cycle 300 times with only slight voltage fluctuations even at 5 mA cm^{-2}, manifesting good reversibility. The long lifespan of solid-state ZABs with SSM/Co_4N/CoNC cathode exceeded many previously reported works (Figure 7e, Table S4). The photo shown in Figure 7d exemplified that two solid-state ZABs with SSM/Co_4N/CoNC cathode united in series could supply a set of LED, demonstrating its potential in practical devices. All these results revealed the solid-state ZAB with SSM/Co_4N/CoNC would be a promising power source for advanced electronic devices in the future, specifically flexible and wearable devices.

3. Conclusion

In summary, we in-situ anchored the Co-N-C Nanoparticles on Co_4N nanosheets towards a flexible self-supported bifunctional SSM/Co_4N/CoNC cathode by a facile and scalable strategy. Due to the binder-free feature, constructed hierarchically porous architectures, abundant active sites, as well as the synergistic effects between Co-N-C and Co_4N, the noble metal-free SSM/Co_4N/CoNC oxygen electrocatalyst delivered outstanding bifuntional activities for OER and ORR with a low overpotential and good durability, which also ensured the exceptional performances for rechargeable ZABs. Unexpectedly, the recyclable ZABs reconstituted with used SSM/Co_4N/CoNC, and fresh anode/electrolyte demonstrated a record lifespan of more than 10000 cycles at 20 mA cm^{-2}. In addition, SSM/Co_4N/CoNC endowed ZAB with a fast-charging feature, which could cycle more than 1750 times even charged at 100 mA cm^{-2}. The solid-state ZAB based on the flexible SSM/Co_4N/CoNC cathode displayed reliable stability under different shapes and excellent reversibility for 300 cycles. This work could accelerate the practical application of long-cycling and fast-charging recyclable ZABs, and inspire new avenues to develop flexible electrodes for other renewable energy storage systems.

Supporting Information
Supporting Information is available from the Wiley Online Library or from the author.

Acknowledgements
This work is supported by a grant from Collaborative Research Fund (CRF) (Project no. C5031-20G) of Research Grant Council, University Grant Committee, HK SAR. The authors would like to thank Shiyanjia Lab (www.shiyanjia.com) for the support of TEM and BET tests.

Received: ((will be filled in by the editorial staff))
Revised: ((will be filled in by the editorial staff))
Published online: ((will be filled in by the editorial staff))

References

[1] X. Shi, Y. Zuo, P. Zhai, J. H. Shen, Y. Y. W. Yang, Z. Gao, M. Liao, J. X. Wu, J. W. Wang, X. J. Xu, Q. Tong, B. Zhang, B. J. Wang, X. M. Sun, L. H. Zhang, Q. B. Pei, D. Y. Jin, P. N. Chen, H. S. Peng, *Nature* **2021**, *591*, 240.

[2] J. Zhou, J. Cheng, B. Wang, H. Peng, J. Lu, *Energy Environ. Sci.* **2020**, *13*, 1933-1970.

[3] Y.-H. Zhu, X.-Y. Yang, T. Liu, X.-B. Zhang, *Adv. Mater.* **2020**, *32*, 1901961.

[4] T. Liu, Y. Yu, X.-Y. Yang, J. Wang, X.-B. Zhang, *Small Struct.* **2020**, 1, 2000015.

[5] L. Yin, J. Scharf, J. Ma, J.-M. Doux, C. Redquest, V. L. Le, Y. Yin, J. Ortega, X. Wei, J. Wang, Y. S. Meng, *Joule*, **2021**, *5*, 228-248.

[6] Y. B. Li, J. Fu, C. Zhong, T. Wu, Z. Chen, W. Hu, K. Amine, J. Lu, *Adv. Energy Mater.* **2019**, *9*, 1802605.

[7] T. Liu, X.-Y. Yang, X.-B. Zhang, *Adv. Mater. Technol.* **2020**, *5*, 2000476.

[8] J. Fu, J. Zhang, X. Song, H. Zarrin, X. Tian, J. Qiao, L. Rasen, K. Li, Z. Chen, *Energy Environ. Sci.* **2016**, *9*, 663-670.

[9] X. Liu, X. Fan, B. Liu, J. Ding, Y. Deng, X. Han, C. Zhong, W. Hu, *Adv. Mater.* **2021**, 2006461.

[10] W. Sun, F. Wang, B. Zhang, M. Zhang, V. Kuepers, X. Ji, C. Theile, P. Bieker, K. Xu, C. Wang, M. Winter, *Science* **2021**, *371*, 46-51.

[11] S. Zhao, Y. Zuo, T. Liu, S. Zhai, Y. Dai, Z. Guo, Y. Wang, Q. He, L. Xia, C. Zhi, J. Bae, K. Wang, M. Ni, *Adv. Energy Mater.* **2021**, *11*, 2101749.

[12] S. Zhao, T. Liu, Y. Dai, Y. Wang, Z. Guo, S. Zhai, J. Yu, C. Zhi, M. Ni, *Chem. Eng. J.* **2021**, 132718.

[13] Y. Jiang, Y.-P. Deng, R. Liang, J. Fu, R. Gao, D. Luo, Z. Bai, Y. Hu, A. Yu, Z. Chen, *Nat. Commun.* **2020**, *11*, 5858.

[14] L. Yan, Y. Xu, P. Chen, S. Zhang, H. Jiang, L. Yang, Y. Wang, L. Zhang, J. Shen, X. Zhao, L. Wang, *Adv. Mater.* **2020**, *32*, 2003313.

[15] Y. Liu, Y. Zhu, Y. Cui, *Nat. Energy* **2019**, *4*, 540-550.

[16] X. Yan, Y. Ha, R. Wu, *Small Methods* **2021**, 2000827.

[17] M. Wu, G. Zhang, M. Wu, J. Prakash, S. Sun, *Energy Storage Mater.* **2019**, *21*, 253-286.

[18] X. Wang, S.-I. Choi, L. T. Roling, M. Luo, C. Ma, L. Zhang, M. Chi, J. Liu, Z. Xie, J. A. Herron, M. Mavrikakis, Y. Xia, *Nat. Commun.* **2015**, *6*, 7594.

[19] H. Yang, X. Han, A. I. Douka, L. Huang, L. Gong, C. Xia, H. S. Park, B. Y. Xia, *Adv. Funct. Mater.* **2021**, *31*, 2007602.

[20] X. Zhu, C. Hu, R. Amal, L. Da, X. Lu, *Energy Environ. Sci.* **2020**, *13*, 4536-4563.

[21] L. Chen, L. Zhou, H. Lu, Y. Zhou, J. Huang, J. Wang, Y. Wang, X. Yuan, and Y. Yao, *Chem. Commun.* **2020**, *56*, 9138-9141.

[22] J. Wang, K. Li, H. Zhong, D. Xu, Z. Wang, Z. Jiang, Z. Wu, X. Zhang, *Angew. Chem. Int. Ed.* **2015**, *54*, 10530-10534.

[23] G. Wu, K. L. More, C. M. Johnston, P. Zelenay, *Science* **2011**, *332*, 443.

[24] C. Wang, Y. Lu, S. Lu, S. Ma, X. Zhu, Z. Li, Q. Liu, *J. Power Sources* **2021**, *495*, 229782.

[25] P. Yu, L. Wang, F. Sun, Y. Xie, X. Liu, J. Ma, X. Wang, C. Tian, J. Li, H. Fu, *Adv. Mater.* **2019**, *31*, 1901666.

[26] A. Zitolo, N. Ranjbar-Sahraie, T. Mineva, J. Li, Q. Jia, S. Stamatin, G. F. Harrington, S. M. Lyth, P. Krtil, S. Mukerjee, E. Fonda, F, Jaouen, *Nat. Commun* **2017**, *8*, 957.

[27] P. Chen, K. Xu, Z. Fang, Y. Tong, J. Wu, X. Lu, X. Peng, H. Ding, C. Wu, Y. Xie, *Angew. Chem., Int. Ed.* **2015**, *54*, 14710-14714.

[28] H. Ge, G. Li, J. Shen, W. Ma, X. Meng, L. Xu, *Appl. Catal. B: Environ.* **2020**, *275*, 119104.

[29] Y. Guo, P. Yuan, J. Zhang, Y. Hu, I. S. Amiinu, X. Wang, J. Zho, H. Xia, Z. Song, Q. Xu, S. Mu, *ACS Nano* **2018**, *12*, 1894-1901.

[30] C. Tang, B. Wang, H.-F. Wang, Q. Zhang, *Adv. Mater.* **2017**, *29*, 1703185.

[31] H.-F. Wang, L. Chen, H. Pang, S. Kaskel, Q. Xu, *Chem. Soc. Rev.* **2020**, *49*, 1414-1448.

[32] P. Zhang, F. Sun, Z. Xiang, Z. Shen, J. Yun, D. Cao, *Energy Environ. Sci.* **2014**, *7*, 442-450.

[33] W. Xia, A. Mahmood, R. Zou, Q. Xu, *Energy Environ. Sci.* **2015**, *8*, 1837-1866.

[34] H. B. Wu, X. W. Lou, *Sci. Adv.* **2017**, *3*, eaap9252.

[35] H. Zhong, K. Li, Q. Zhang, J. Wang, F. Meng, Z. Wu, J. Yan, X. Zhang, *NPG Asia Mater.* **2016**, *8*, e308-e308.

[36] D. Ji, L. Fan, L. Li, S. Peng, D. Yu, J. Song, S. Ramakrishna, S. Guo, *Adv. Mater.* **2019**, *31*, 1808267.

[37] C. Niu, J. Liu, T. Qian, X. Shen, J. Zhou, C. Yan, *Natl. Sci. Rev.* **2020**, *7*, 315-323.

[38] Y. Wang, Q. Cao, C. Guan, C. Cheng, *Small* **2020**, *16*, 2002902.

[39] Z. Ma, P. Pei, K. Wang, X. Wang, H. Xu, Y. Liu, G. Peng, *J. Power Sources* **2015**, *274*, 56-64.

[40] M. Wu, G. Zhang, N. Chen, W. Chen, J. Qiao, S. Sun, *Energy Storage Mater.* **2020**, *24*, 272-280.

[41] J. Duan, S. Chen, S. Dai, S. Z. Qiao, *Adv. Funct. Mater.* **2014**, *24*, 2072-2078.

[42] T.-H. Gu, D. A. Agyeman, S.-J. Shin, X. Jin, J. M. Lee, H. Kim, Y.-M. Kang, S.-J. Hwang, *Angew. Chem. Int. Ed.* **2018**, *57*, 15984-15989.

[43] H.-X. Zhong, J. Wang, Q. Zhang, F. L. Meng, D. Bao, T. Liu, X.-Y. Yang, Z.-W. Chang, J.-M. Yan, X.-B. Zhang, *Adv. Sustainable Syst.* **2017**, *1*, 1700020.

[44] Z. Li, M. Shao, L. Zhou, R. Zhang, C. Zhang, M. Wei, D. G. Evans, X. Duan, *Adv. Mater.* **2016**, *28*, 2337-2344.

[45] G. Cai, W. Zhang, L. Jiao, S.-H. Yu, H.-L. Jiang, *Chem*, **2017**, *2*, 791-802.

[46] X. Zhu, T. Jin, C. Tian, C. Lu, X. Liu, M. Zeng, X. Zhuang, S. Yang, L. He, H. Liu, S. Dai, *Adv. Mater.* **2017**, *29*, 1704091.

[47] Z. Chen, Y. Song, J. Cai, X. Zheng, D. Han, Y. Wu, Y. Zang, S. Niu, Y. Liu, J. Zhu, X. Liu, G. Wang, *Angew. Chem. Int. Ed.* **2018**, *57*, 5076-5080.

[48] L.-N. Song, W. Zhang, Y. Wang, X. Ge, L.-C. Zou, H.-F. Wang, X.-X. Wang, Q.-C. Liu, F. Li, J.-J. Xu, *Nat. Commun.* **2020**, *11*, 2191.

[49] P. E. Marchezi, E. M. Therézio, R. Szostak, H. C. Loureiro, K. Bruening, A. Gold-Parker, M. A. M. Jr., C. J. Tassone, H. C. N. Tolentino, M. F. Toney, A. F. Nogueira, *J. Mater. Chem. A* **2020**, *8*, 9302-9312.

[50] Q. Xu, H. Jiang, Y. Li, D. Liang, Y. Hu, C. Li, Appl. Catal. B: Environ. **2019**, *256*, 117893.

[51] K. R. Yoon, K. Shin, J. Park, S.-H. Cho, C. Kim, J.-W. Jung, J. Y. Cheong, H. R. Byon, H. M. Lee, I.-D. Kim, *ACS Nano* **2018**, *12*, 128-139.

[52] T. Liu, M. Li, X. Bo, M. Zhou, *ACS Sustainable Chem. Eng.* **2018**, *6*, 11457-11465.

[53] N. Li, D. K. Bediako, R. G. Hadt, D. Hayes, T. J. Kempa, F. von Cube, D. C. Bell, L. X. Chen, D. G. Nocera, *Proc. Natl. Acad. Sci. USA* **2017**, *114*, 1486.

[54] D. Guo, R. Shibuya, C. Akiba, S. Saji, T. Kondo, J. Nakamura, *Science* **2016**, *351*, 361-365.

[55] J. Zhang, J. Chen, Y. Luo, Y. Chen, Z. Li, J. Shi, G. Wang, R. Wang, *Carbon* **2020**, *159*, 16-24.

[56] Z. Chen, X. Yang, W. Li, X. Liang, J. Guo, H. Li, Y. He, Y. Kim, *Small* **2021**, *17*, 2103048.

[57] Q. Zhang, J. Luan, X. Huang, L. Zhu, Y. Tang, X. Ji, H. Wang, *Small* **2020**, *16*, 2000929.

[58] H.-P. Li, X.-Y. Ji, J.-J. Liang, *Rare Met.* **2020,** *39*, 861-862.

[59] K.-C. Pu, X. Zhang, X.-L. Qu, J.-J. Hu, H.-W. Li, M.-X. Gao, H.-G. Pan, Y.-F. Liu, *Rare Met.* **2020**, *39*, 616-635.

[60] J. Liu, Y. Cao, J. Zhou, M. Wang, H. Chen, T. Yang, Y. Sun, T. Qian, C. Yan, *ACS Appl. Mater. Interfaces* **2020**, *12*, 54537-54544.

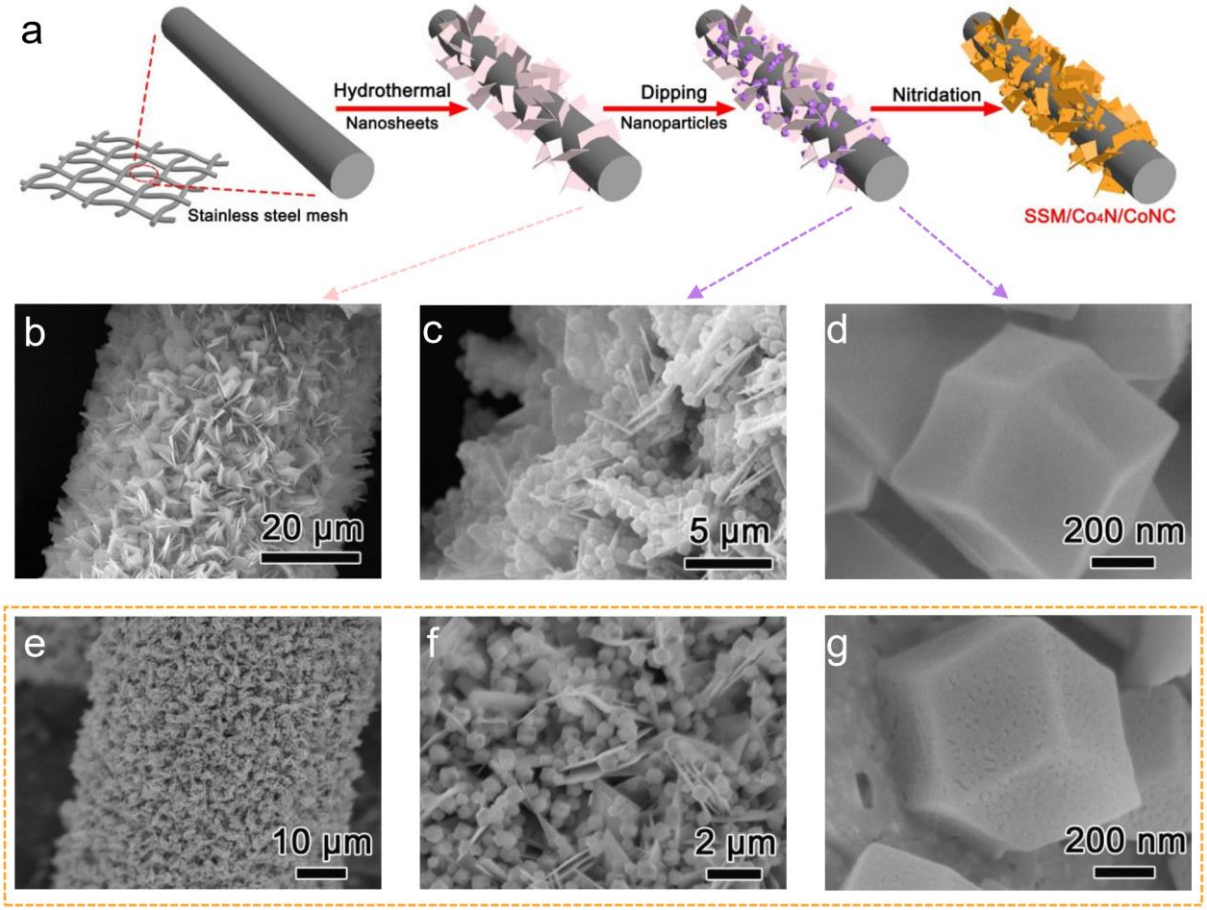

Figure 1. a) Schematic of the synthesis procedure of SSM/Co_4N/CoNC. SEM images of b) nanosheets grown on SSM, and c,d) ZIF-67 nanoparticles in-situ grown on nanosheets. e-g) SEM images of SSM/Co_4N/CoNC oxygen electrode after nitridation at 400 °C.

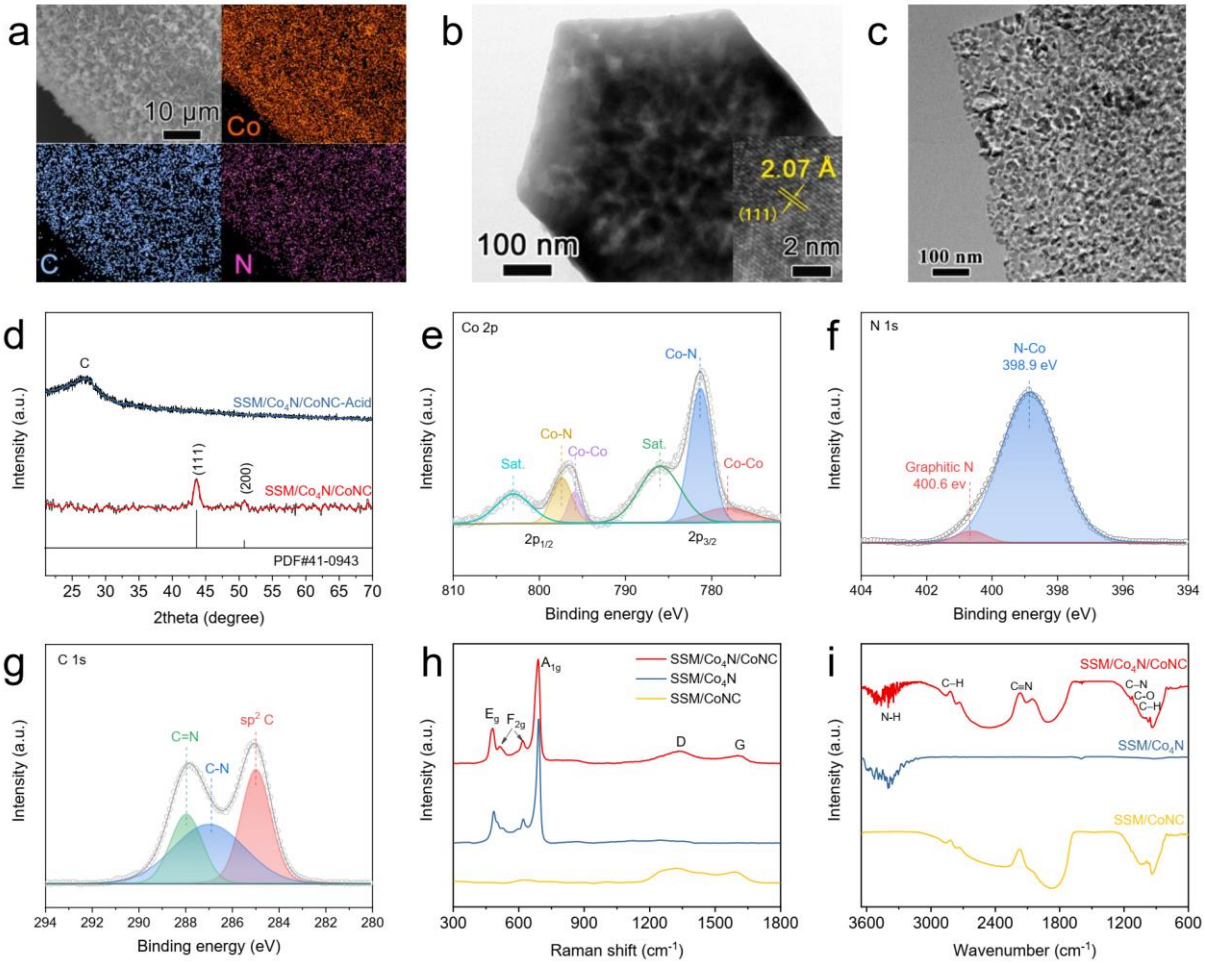

Figure 2. a) Element mapping of Co, C, and N, and b,c) TEM and HRTEM (inset) images of SSM/Co_4N/CoNC. d) XRD patterns for SSM/Co_4N/CoNC powders and SSM/Co_4N/CoNC-Acid. e) Co 2p, f) N 1s, g) O 1s XPS spectra of SSM/Co_4N/CoNC. h) Raman spectrum and i) FTIR spectrum of SSM/Co_4N/CoNC, SSM/Co_4N, SSM/CoNC.

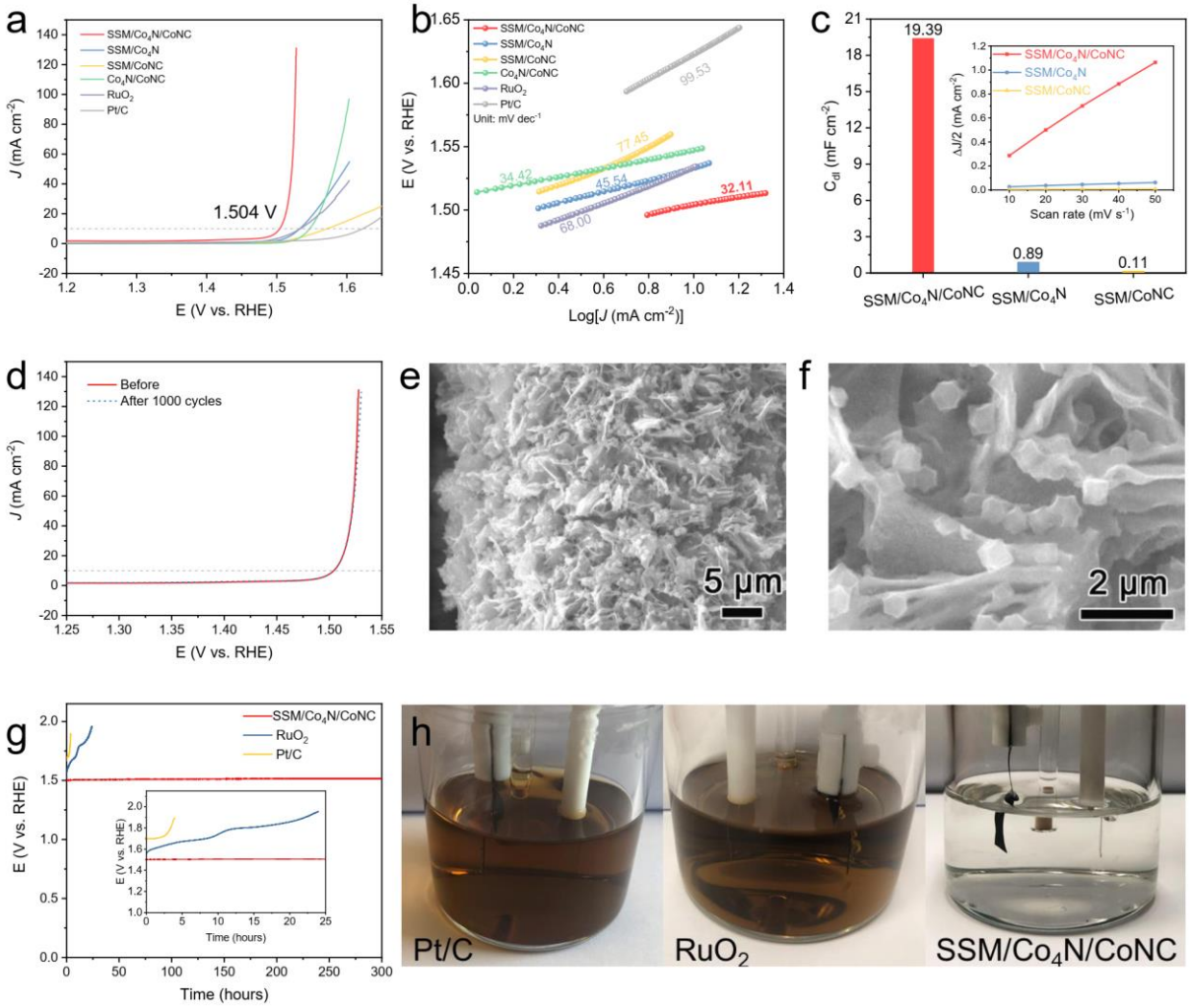

Figure 3. a) Polarization curves for OER, b) corresponding Tafel slopes, and c) comparison of C_{dl} for selected electrode, inset is the curves of capacitive currents vs. scan rates. d) Polarization curves of SSM/Co_4N/CoNC before and after 1000 cycles for OER test. e,f) SEM images of SSM/Co_4N/CoNC electrode after 1000 cycles. g) OER durability. h) Photographs of electrolyte solutions for selected electrodes after long term stability tests.

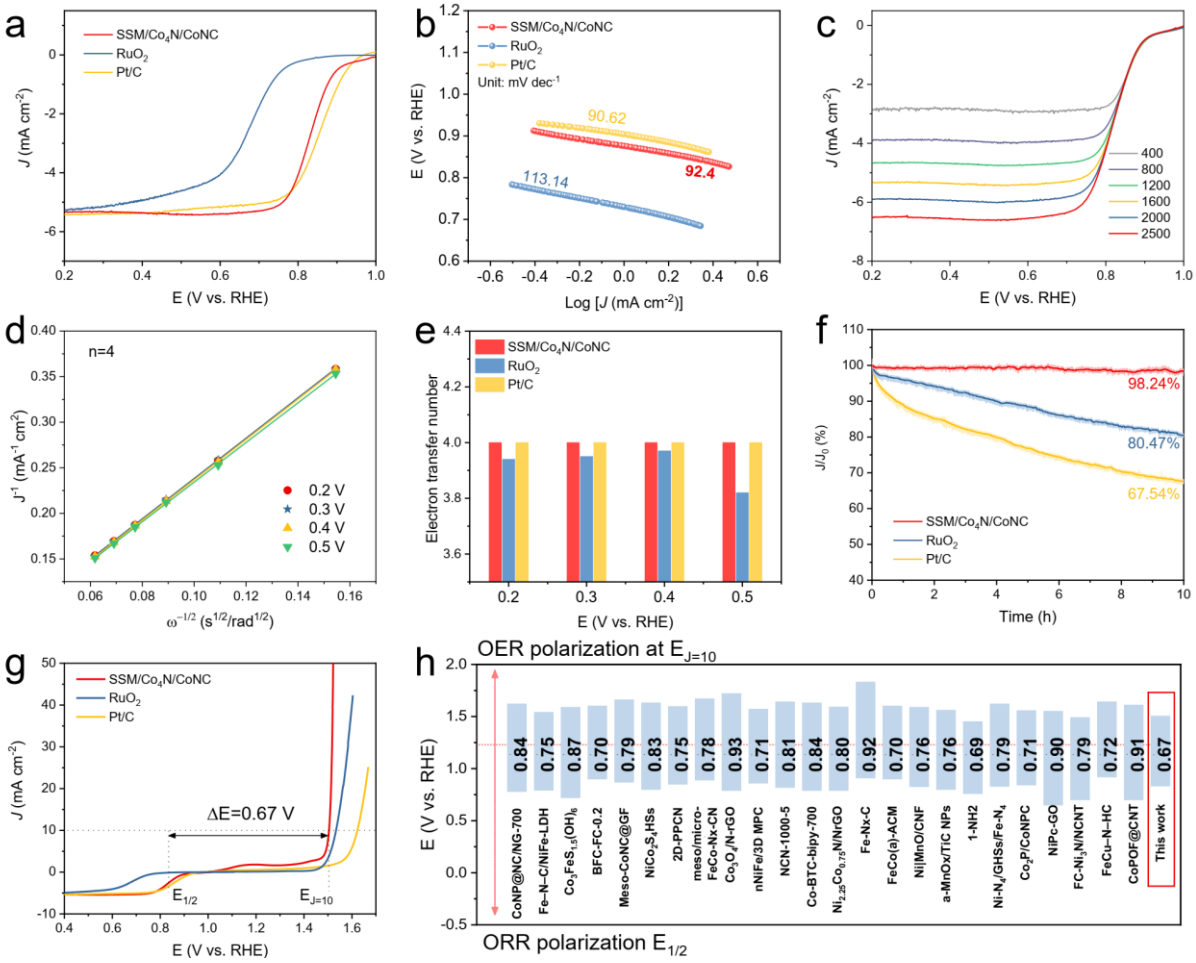

Figure 4. a) Polarization curves, b) Tafel slopes for SSM/Co4N/CoNC, Pt/C and RuO_2. c) LSV curves at different rotating speeds and d) the corresponding Koutecky-Levich plots at different potentials for SSM/Co4N/CoNC. e) Comparison of electron transfer number and f) chronoamperometric response of ORR for selected electrodes. g) Overall polarization curves. h) Comparison of ΔE values for SSM/Co4N/CoNC with published bifunctional cathodes.

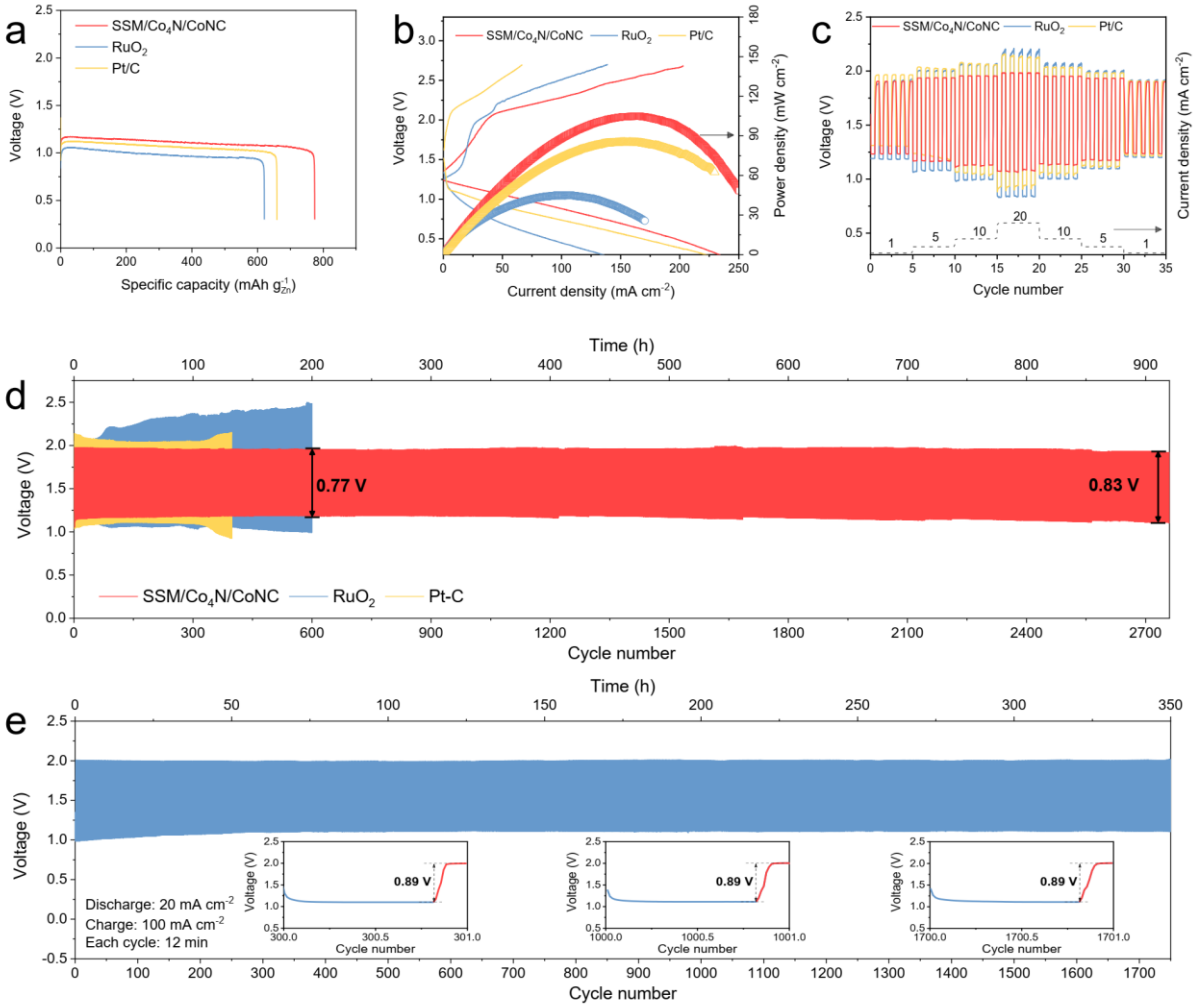

Figure 5. a) Galvanostatic discharge voltage-capacity curves at 10 mA cm^{-2}, b) polarization curves and power density curves, c) cycling curves at different current densities, and d) galvanostatic cycling curves at 10 mA cm^{-2} for the ZABs with SSM/Co_4N/CoNC, RuO_2, and Pt/C cathodes. e) Fast-charging cycling performance of SSM/Co_4N/CoNC-based ZABs.

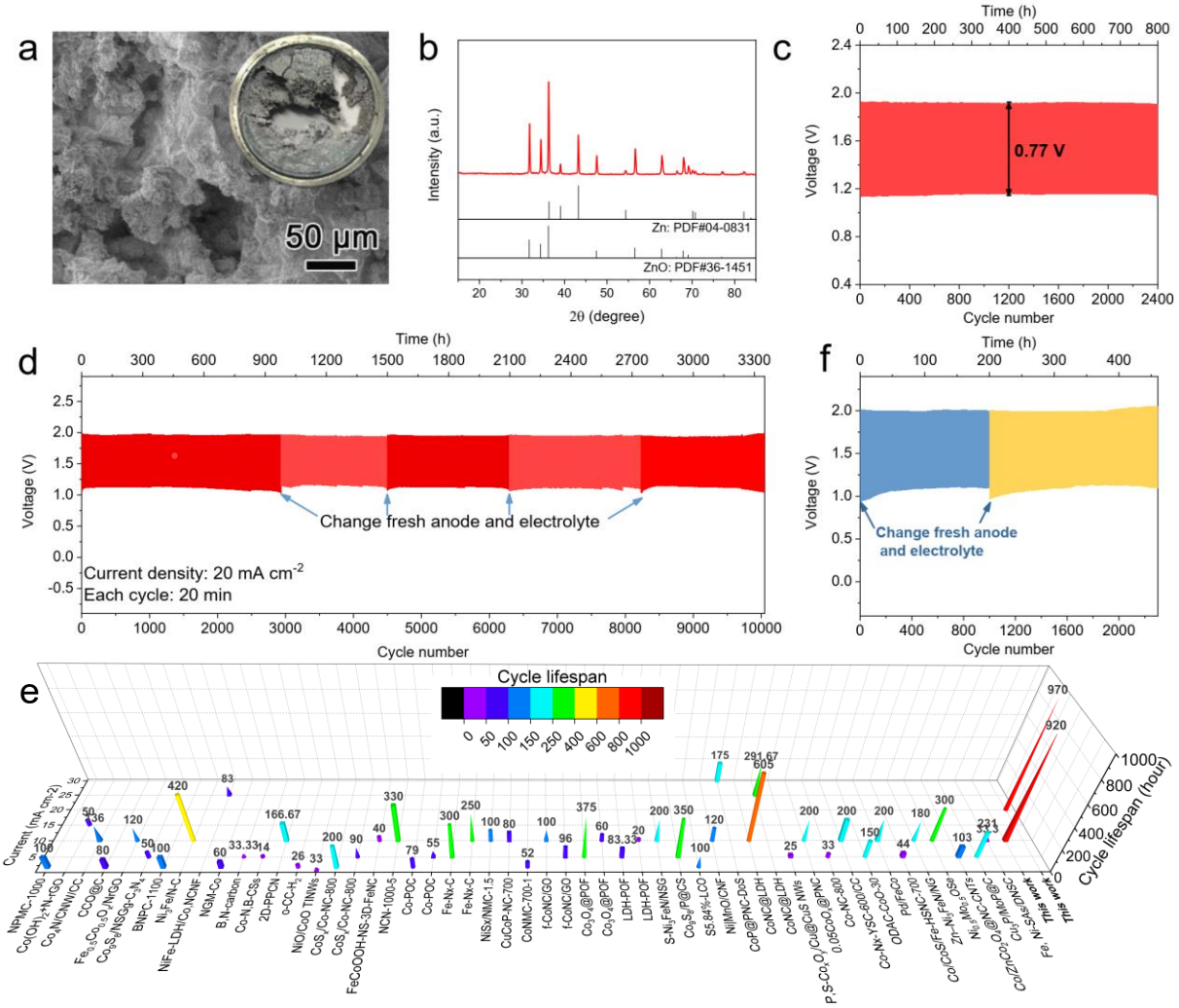

Figure 6. a) SEM image and photograph (inset) of Zn anode after over 2700 cycles in the ZAB, and b) the corresponding XRD curve. c) The cycling curve of the rebuilt ZAB at 10 mA cm^{-2}. d) Galvanostatic cycling curves of the recyclable ZABs reconstituted with recovered SSM/Co_4N/CoNC and fresh anode/electrolyte at 20 mA cm^{-2}. e) Comparison of rechargeable ZAB performance for SSM/Co_4N/CoNC and other reported cathodes regarding current density and cycling lifespan. f) The cycling curve of the rebuilt fast-charging ZAB with the recycled SSM/Co_4N/CoNC cathode (after 1750 cycles) and fresh Zn anode and electrolyte, discharging at 20 mA cm^{-2} and charging at 100 mA cm^{-2}.

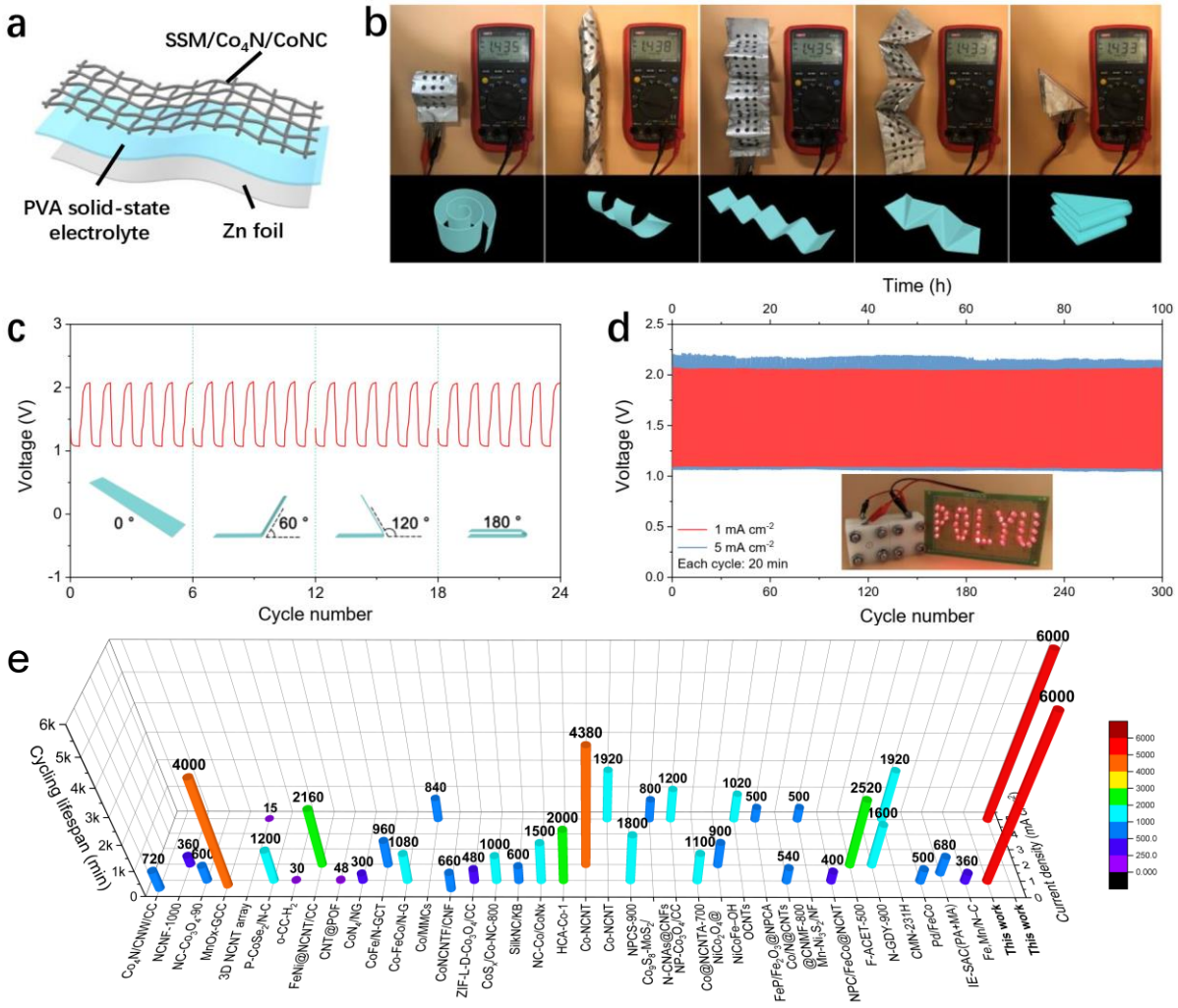

Figure 7. a) Structural schematic of flexible solid-state rechargeable ZAB. b) Open-circuit voltage of the flexible ZAB at different bended conditions. c) Discharge-charge curves of flexible ZAB under different bending angles at current density of 1 mA cm^{-2}. d) Cycling curves of the SSM/Co_4N/CoNC-based solid-state ZAB. e) Comparison of solid-state ZAB performance for SSM/Co_4N/CoNC and other reported cathodes regarding current density and cycling lifespan.

An ultrastable flexible self-supported bifunctional cathode was fabricated via a facile and effective strategy, in which the highly active Co_4N and Co-N-C were elaborately bridged together. Their synergistic effect and delicate structure lead to a breakthrough for recyclable Zn-air batteries, give a lifespan of more than 10000 cycles, and a fast-charging feature.

Tong Liu, Siyuan Zhao, Ying Wang, Jie Yu, Yawen Dai, Jian Wang, Xiaoxu Sun, Kaihua Liu, Meng Ni

In-Situ Anchoring Co-N-C Nanoparticles on Co_4N Nanosheets towards Ultrastable Flexible Self-Supported Bifunctional Oxygen Electrocatalyst Enables Recyclable Zn-Air Batteries over 10000 Cycles and Fast-Charging